Output-Impedance Shaping of Bidirectional DAB DC–DC Converter Using Double-Proportional-Integral Feedback for Near-Ripple-Free DC Bus Voltage Regulation in Renewable Energy Systems

Lingling Cao, *Student Member, IEEE*, K. H. Loo, *Member, IEEE*, and Y. M. Lai, *Member, IEEE*

***Abstract*—This paper investigates the design and implementation of virtual-output-impedance shaping on an inverter-loaded, fuel-cell-battery-powered dc–dc converter system for achieving near-ripple-free dc bus voltage regulation. The method is based on the insertion of a second output-voltage feedback loop as can be inferred from the Mason's gain formula. Three basic modes of virtual-output-impedance shaping (proportional, derivative, integral) are discussed and the closed-loop output-impedance characteristics due to each of them are analyzed in detail and with their Thévenin equivalent circuits derived. Despite the suitability of integral feedback for minimizing converter's output impedance, it can give rise to an unwanted resonance peak near the converter's crossover frequency, thus potentially destabilizing the system. The solution to the problem using combination of basic virtual-output-impedance shaping modes and its practical implementation are discussed. When implemented on a fuel-cell-battery-powered dual-active-bridge dc–dc converter, the second-harmonic distortion of dc bus voltage is shown to have been reduced by 85.5% compared to a conventionally PI-compensated system.**

***Index Terms*—Bidirectional converters, DC-DC converters, dual active bridge, energy storages, fuel cells, outputimpedance shaping.**

I. Introduction

SINGLE-INPUT and multi-input dual-active-bridge (DAB) dc–dc converter topology has been gaining popularity for renewable energy system applications due to its bidirectional power transfer capacity, particularly for interfacing energy storage devices such as batteries and super-capacitors to dc voltage bus in hybrid energy systems involving slow-response or ripple-sensitive renewable energy sources. For this converter topology and its derivatives, power flow is typically controlled by phase-shifting transformer's primary voltage with respect to its secondary voltage. This bidirectional topology possesses the advantages of flexible power flow control, zero-voltage-switching (ZVS) operation, high efficiency, good modularity, and symmetrical (with respect to forward and reverse power flow) structure.

Many variants of DAB dc–dc converter topology have been proposed, among which full-bridge isolated bidirectional DAB dc–dc converter is the most studied topology. Besides the basic phase-shift control [1]–[2], extended-phase-shift [3]–[5], dual-phase-shift [6], and even triple-phase-shift [7]–[12] control have been proposed and implemented to improve converter's efficiency and expand ZVS operating region when transformer's primary and secondary voltage amplitudes are not matched. For medium-power applications, half-bridge topology is advantageous due to low-component count and simpler control. Besides the commonly used phase-shift control, asymmetrical duty-cycle control has also been proposed to extend DAB converter's soft-switching operating range [13]. A series of further improvements, including more accurate dynamic models [14]–[16], improvement of efficiency at light load [17], optimization of transformer design [18], and advanced magnetic and device materials [19] have also been reported in the literature.

In previous researches, various multiport converter system structures have been proposed for renewable energy systems supported by energy storages. Generally, they can be classified into three types of structure depending on the interfacing position of energy storage: 1) high-voltage dc link [20]–[21]; 2) low-voltage dc link [22]–[31]; and 3) transformer coupling [32]–[36]. For structure 1, renewable energy sources and energy storages are interfaced to the high-voltage dc link through unidirectional and bidirectional converters, respectively. This type of modular design approach provides easier maintenance and better extensibility, although it suffers from the drawbacks of increased cost, size, and volume. For structure 2, multiport converter topologies are derived from conventional half-bridge or full-bridge converter with the provision of a third port (directly or through switches) for interfacing energy storages to the low-voltage dc link. A systematic derivation of three-port converters from half-bridge and full-bridge converter is given in [29] and [30], respectively, offering the benefits of reduced cost and higher power density. For these topologies, the control design for realizing various operating modes and seamless mode transition are the main challenges [31]. Finally, for structure 3, instead of being tied a common dc link, renewable energy sources and energy storages are coupled through a common

Manuscript received February 9, 2015; revised April 16, 2015; accepted May 11, 2015. Date of publication May 14, 2015; date of current version November 16, 2015. This work was supported by the University Grants Committee of the Hong Kong Special Administrative Region, Research Grants Council, under Earmarked Research Grant PolyU 5193/10 and Grant PolyU 5390/13. Recommended for publication by Associate Editor Y. Xing.

The authors are with the Department of Electronic and Information Engineering, The Hong Kong Polytechnic University, Hong Kong (e-mail: lingling.cao@connect.polyu.hk; kh.loo@polyu.edu.hk; enymlai@polyu.edu.hk).

Color versions of one or more of the figures in this paper are available online at http://ieeexplore.ieee.org.

Digital Object Identifier 10.1109/TPEL.2015.2433535

multiwinding transformer [32]–[36]. However, the main drawback of this approach is that it leads to more complicated control.

Among the various structures discussed above, structure 1 is adopted in our study. The first input, comprising ripple-sensitive renewable energy source, is controlled as power or current source and the second input, comprising fast-response energy storage, is controlled as voltage source for regulating the dc bus voltage by means of responding to all power changes that cannot be met by the renewable energy source. Due to the high-output-impedance nature of the dc–dc converter associated with the renewable energy source, the dc–dc converter associated with the energy storage should introduce ideally a zero-impedance path to the flow of any transient power not met by the renewable energy source. Specifically in a renewable energy system loaded with inverter, the periodically varying load power at twice the inverter frequency will cause the existence of second-harmonic component on the system's dc bus voltage. If the output impedance of the energy storage branch is inappropriately designed and a significant amount of second-harmonic current is drawn from the ripple-sensitive renewable energy source, it can shorten the lifetime of the energy source. The problem can be mitigated if large dc-link capacitor is placed across the dc bus, but minimizing the size of the second-harmonic component for high-power systems will typically require an excessively large dc-link capacitor. Solving the problem through the design of the energy storage branch's output impedance remains the most promising and economical solution.

In the authors' previous work [38], a systematic analysis of a family of output-impedance shaping methods inferred from the Mason's gain formula was presented. Four basic modes of output-impedance shaping methods, namely feedforward of load current and feedback of output voltage in three different forms (proportional, derivative, integral), were derived, analyzed, and verified experimentally. All other impedance shaping methods are essentially derivatives or combinations of these four basic modes. It has been demonstrated in [38] that the utilization of load-current feedforward simply introduces a dc offset in the magnitude of the converter's closed-loop output impedance without altering its frequency response, which makes its analysis and design straightforward. This, unfortunately, is not true for the other three basic modes based on output-voltage feedback. As a second feedback loop is added to the converter's control system, it is deemed to interact with the existing feedback loop in the original system and give rise to various closed-loop output-impedance characteristics. The nature of these interactions and the way with which they affect the closed-loop output-impedance design of the converter are important issues from the viewpoint of their application in renewable energy systems involving ripple-sensitive energy sources. While the previous work [38] formulated the framework of power converter's output-impedance shaping methods based on the Mason's gain formula, the current study emphasizes on the design-oriented analysis and application of these methods for practical system design.

This paper discusses the application of the previously developed virtual-output-impedance shaping technique in renewable energy system involving ripple-sensitive energy source. Specifically, it aims to address the problem of second-harmonic distortion of the dc bus voltage of a fuel cell power conditioning system based on the well-researched and widely used multi-input bidirectional DAB dc–dc converter architecture, and its minimization based on the consideration of the output-impedance design of the energy storage branch. In contrary to the previous work [38], the output-impedance characteristics resulting from each of the three forms of output-voltage feedback are discussed from a closed-loop perspective. It will be shown that, among the three basic modes, integral feedback represents the most appropriate form of output-impedance shaping for the stated application, but at the same time it is also found to degrade the converter's stability and voltage regulation performance by creating a virtual inductor that resonates with the converter's output capacitor. A feasible and practical solution is reached by combining multiple basic modes of output-impedance shaping in appropriate way, as will be discussed later in this paper.

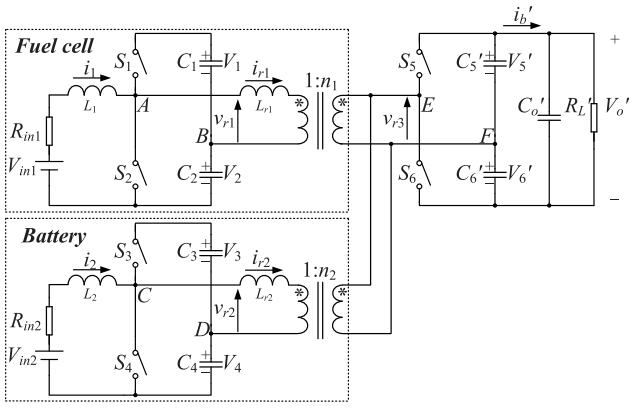

Fig. 1. Multi-input bidirectional DAB dc–dc converter with shared secondary half-bridge cell.

To achieve these objectives, Section II of the paper presents a brief review of the multi-input bidirectional DAB dc–dc converter system. This is followed by a thorough closed-loop output-impedance analysis in Section III focusing on the three basic modes of output-impedance shaping derived from output-voltage feedback. Design equations are presented to facilitate their application in a practical system design. The problem of resonant peak generated by integral feedback and the method for damping its effect are also presented here. Section IV discusses the practical implementation of the solution, which is verified experimentally in Section V with the presentation and discussion of converter's steady-state and dynamic waveforms and the fast Fourier transform (FFT) analysis of dc bus voltage. Finally, the paper is concluded in Section VI.

II. Multi-Input Bidirectional DAB DC–DC Converter

Fig. 1 shows a multi-input bidirectional DAB dc–dc converter [37] that employs two separate transformers for achieving independent control of each input half-bridge cell, which facilitates the implementation of various power-flow control strategies for

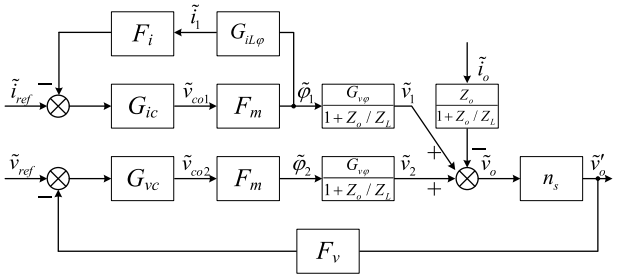

Fig. 2. Control block diagram for the multi-input bidirectional DAB dc–dc converter shown in Fig. 1.

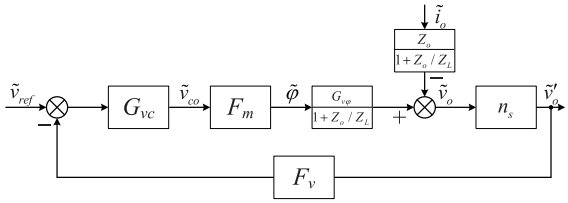

Fig. 3. Basic control system of the DAB dc–dc converter associated with the energy storage branch.

the fuel cell power conditioning system. Referring to Fig. 1, $v_{r1} \sim v_{r2}$, and v_{r3} represents the output voltages of the two input half-bridge cells and the shared secondary half-bridge cell, respectively. The capacitors $C_1 \sim C_4$ and $C_5' \sim C_6'$ are assumed to be sufficiently large that the voltages $V_1 \sim V_4$ and $V_5' \sim V_6'$ are assumed to be constant. The currents flowing through the transformer's leakage inductance of input half-bridge cells 1 and 2 are denoted by i_{r1} and i_{r2}, respectively.

By using phase-shift control, the power flow of each input half-bridge cell can be controlled by adjusting the phase difference (φ_1 or φ_2) between the transformer's primary and secondary voltages. According to the control strategies discussed above, the fuel cell branch always delivers power by controlling φ_1 to be larger than zero, while the energy storage branch can be controlled to deliver power ($\varphi_2 > 0$), absorb power ($\varphi_2 < 0$), or have no contribution to the load ($\varphi_2 = 0$) by adjusting the value of φ_2. For the two-input converter shown in Fig. 1, the power delivered by the fuel cell and energy storage, and the total power delivered by both, is given by (1)–(3), respectively,

$$P_f = \frac{\int_0^{2\pi} i_{r1}(\theta)v_{r1}(\theta)d\theta}{2\pi} = \frac{\varphi_1\,(\pi - |\varphi_1|)}{4\pi\omega L_{r1}}\frac{V_{12}V_{56}'}{n_1} \quad (1)$$

$$P_b = \frac{\int_0^{2\pi} i_{r2}(\theta)v_{r2}(\theta)d\theta}{2\pi} = \frac{\varphi_2\,(\pi - |\varphi_2|)}{4\pi\omega L_{r2}}\frac{V_{34}V_{56}'}{n_2} \quad (2)$$

$$P_o = P_f + P_b \quad (3)$$

where $V_{12} = (V_1 + V_2)$, $V_{34} = (V_3 + V_4)$, and $V_{56}' = (V_5' + V_6') = V_o'$.

On the control strategy for the multi-input converter system, the fuel cell branch is controlled to deliver a constant current while the energy storage branch is responsible for regulating the dc-bus voltage. The full control block diagram is shown in Fig. 2, where n_s is the transformer's turn ratio, F_v and F_i are the sampling gains of the dc bus voltage and fuel cell's output current, respectively, $\tilde{v}_{\rm ref}$ and $\tilde{i}_{\rm ref}$ are the reference signals for the dc bus voltage and fuel cell's output current, respectively, $G_{\rm vc}$ and $G_{\rm ic}$ are the compensation network's gain of the output-voltage and fuel-cell-current feedback loop, respectively, $\tilde{v}_{\rm co}$ is the control signal, and F_m is the modulator's gain. The small-signal transfer functions of the two-input converter have been analyzed in detail in [37] and [38]. Specifically, the control-to-output-current transfer function $G_{i\varphi}$, which is frequently used in the following analysis, is repeated here and given by (4). For a given nominal input voltage $V_{\rm in}$, switching frequency ω, phase difference φ, and transformer's leakage inductance L_r, the transfer function can be approximated as being constant. The designation i_b is used instead of i_b' to denote the output current reflected to the transformer's primary side

$$\frac{\tilde{i}_b}{\tilde{\varphi}} = \frac{V_{in}}{2\pi\omega L_r}\,(\pi - 2\,|\varphi|) = G_{i\varphi}. \quad (4)$$

Thus, by making the substitutions $Z_o = 1/sC_o$ and $Z_L = R_L$, where C_o is the total dc-link capacitor ($= n_s^2\,[C_5'C_6'/(C_5' + C_6') + C_o']$) and R_L is the load resistance, both reflected to the transformer's primary side, the small-signal open-loop converter's output voltage $\tilde{v}_o$ is given by (5) in terms of the perturbations in phase difference ($\tilde{\varphi}$) and load current ($\tilde{i}_o$). Here, $G_{v\varphi}$ represents the converter's unloaded ($Z_L \to \infty$) control-to-output-voltage transfer function

$$\begin{aligned}\tilde{v}_o &= (Z_L||Z_o)\,\tilde{i}_b - (Z_L||Z_o)\,\tilde{i}_o \\ &= \frac{G_{i\varphi}Z_o}{1 + Z_o/Z_L}\tilde{\varphi} - \frac{Z_o}{1 + Z_o/Z_L}\tilde{i}_o \\ &= \frac{G_{v\varphi}}{1 + Z_o/Z_L}\tilde{\varphi} - \frac{Z_o}{1 + Z_o/Z_L}\tilde{i}_o. \end{aligned} \quad (5)$$

III. Closed-Loop Output-Impedance Analysis

A. Without Virtual-Output-Impedance Shaping

Fig. 3 shows the basic voltage-loop control system of the bidirectional DAB dc–dc converter associated with the energy storage branch. The system can be visualized as having two inputs, $\tilde{v}_{\rm ref}$ and $\tilde{i}_o$, and one output $\tilde{v}_o$. From Fig. 3, the output voltage $\tilde{v}_o$ produced by the closed-loop system is given by (6), where L is the converter's loop gain

$$\begin{aligned}\tilde{v}_o &= \frac{G_{vc}F_m\frac{G_{v\varphi}}{1+Z_o/Z_L}}{1+L}\tilde{v}_{\rm ref} - \frac{\frac{Z_o}{1+Z_o/Z_L}}{1+L}\tilde{i}_o \\ &= G_{vr}\tilde{v}_{\rm ref} - Z_\Theta\tilde{i}_o \\ L &= G_{vc}F_mF_vn_s\frac{G_{v\varphi}}{1+Z_o/Z_L}. \end{aligned} \quad (6)$$

Consider a typical converter with output voltage regulated using proportional-integral (PI) controller, the converter's closed-loop output impedance Z_Θ can be evaluated by substituting

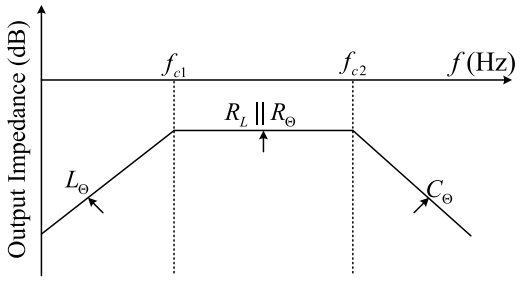

Fig. 4. Closed-loop output impedance of DAB dc–dc converter implemented with PI control.

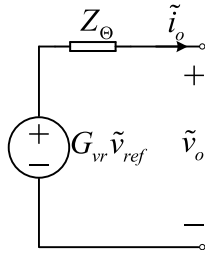

Fig. 5. Equivalent circuit of DAB dc–dc converter implemented with PI control.

$G_{vc} = K_p + K_i/s$ into the second term of (6)

$$\begin{aligned} Z_\Theta &= \frac{\frac{Z_o}{1+Z_o/Z_L}}{1+L} \\ &= \frac{\frac{Z_o}{1+Z_o/Z_L}}{1+\left(K_p+\frac{K_i}{s}\right)F_m F_v n_s \frac{G_{v\varphi}}{1+Z_o/Z_L}} \\ &= \frac{1}{\frac{1}{Z_L}+\frac{1}{Z_o}+K_p F_m F_v n_s G_{i\varphi}+\frac{K_i F_m F_v n_s G_{i\varphi}}{s}} \\ &= \frac{1}{\frac{1}{Z_L}+\frac{1}{Z_{\Theta-C}}+\frac{1}{Z_{\Theta-R}}+\frac{1}{Z_{\Theta-L}}} \end{aligned} \tag{7}$$

where

$$\begin{aligned} Z_L &= R_L \\ Z_{\Theta-C} &= \frac{1}{sC_\Theta} = \frac{1}{sC_o} = Z_o \\ Z_{\Theta-R} &= R_\Theta = \frac{1}{K_p F_m F_v n_s G_{i\varphi}} \\ Z_{\Theta-L} &= sL_\Theta = \frac{s}{K_i F_m F_v n_s G_{i\varphi}}. \end{aligned} \tag{8}$$

Equation (7) shows that by introducing PI compensation to the converter's output-voltage feedback loop, its closed-loop output impedance has been modified from the parallel combination of R_L and $1/sC_o$ to the parallel combination of R_L, R_Θ, L_Θ, and C_Θ. As a result, the output impedance of a PI-controlled DAB dc–dc converter is inductive (dominated by L_Θ) at low frequencies, resistive (dominated by $R_L||R_\Theta$) at mid-range frequencies, and capacitive (dominated by C_Θ) at high frequencies. The lower (f_{c1}) and upper (f_{c2}) corner frequencies are given by (9). As expected, for frequencies below the converter's loop gain's crossover frequency f_{c2}, the converter's closed-loop output impedance is always smaller than its open-loop output impedance since $[R_L||R_\Theta||(sL_\Theta)||(1/sC_\Theta)] < [R_L||(1/sC_o)]$ with $R_\Theta > 0$ and $L_\Theta > 0$. The form of closed-loop output impedance of the DAB dc–dc converter is plotted in Fig. 4 and its equivalent circuit is shown in Fig. 5

$$\begin{aligned} f_{c1} &= \frac{L_\Theta}{2\pi\left(R_L||R_\Theta\right)} \\ f_{c2} &= \frac{1}{2\pi\left(R_L||R_\Theta\right)C_\Theta}. \end{aligned} \tag{9}$$

It should be mentioned that, in general, for a reasonably designed power converter, the condition $R_\Theta \ll R_L$ should prevail since any perturbation in load current ($\tilde{i}_o$) should be mainly compensated by the converter in order to minimize the resulting perturbation in output voltage ($\tilde{v}_o$). Thus, based on this assumption, the corner frequencies f_{c1} and f_{c2} can be closely approximated by (10). In addition, since the converter's maximum output impedance occurs between f_{c1} and f_{c2}, the virtual-output-impedance shaping methods presented in the following parts will be utilized mainly to reduce the converter's output impedance in this frequency region. Furthermore, the proportional gain K_p dominates over the integral gain $|K_i/s|$ in this frequency region, thus the condition $G_{vc} \approx K_p$ is assumed

$$\begin{aligned} f_{c1} &\approx \frac{L_\Theta}{2\pi R_\Theta} = \frac{K_p}{2\pi K_i} \\ f_{c2} &\approx \frac{1}{2\pi R_\Theta C_\Theta}. \end{aligned} \tag{10}$$

B. With Virtual-Output-Impedance Shaping

In [38], it was discussed that the addition of a feedback loop from the converter's output voltage $\tilde{v}_o$ to its control voltage $\tilde{v}_{co}$ introduces an equivalent impedance Z_V virtually connected in parallel with the converter's original output impedance. Since the presence of Z_V naturally modifies the converter's overall output impedance, the technique is known as the virtual-output-impedance shaping technique. Although a systematic derivation and analysis of the technique has been presented in [38], it focused only on open-loop analysis and did not consider the effects of closed-loop operation and, more importantly, controller's configuration on the overall performance of output-impedance shaping. Therefore, users must rely on trial-and-error approach and repeated circuit simulations in order to determine the optimum design parameters for meeting the desired performance specifications. In this section, a systematic analysis of the three basic modes of output-impedance shaping method (proportional, derivative, and integral feedback) will be thoroughly presented from the viewpoint of closed-loop operation. Before the individual modes are discussed, a general formulation of the converter's output impedance in terms of the feedback gain H_{fb}, which can assume any of the three basic forms, is first presented.

Fig. 6 shows the modified control system (with virtual-output-impedance shaping) of the DAB dc–dc converter associated with

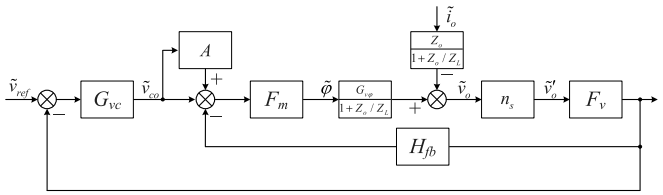

Fig. 6. Modified control system (with virtual-output-impedance shaping) of the DAB dc–dc converter associated with the energy storage branch.

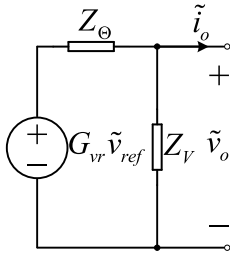

Fig. 7. Equivalent circuit of DAB dc–dc converter implemented with PI control and virtual-output-impedance shaping.

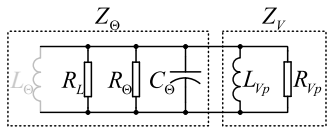

Fig. 8. Equivalent circuit of DAB dc–dc converter implemented with PI control and proportional output-voltage feedback.

the energy storage branch, where the additional feedback gain H_{fb} and the additional forward-path gain A have been added. The insertion of A is to ensure that the additional feedback gain H_{fb} only modifies the output impedance of the converter without affecting its reference-to-output-voltage transfer function. By setting $A = L_{fb} = H_{fb}F_mF_vn_sG_{v\varphi}/(1+Z_o/Z_L)$, where L_{fb} is the loop gain of the additional feedback loop, it can be shown that the converter's output voltage $\tilde{v}_o$ is given by

$$\begin{aligned}\tilde{v}_o &= \frac{(1+A)G_{vc}F_m\frac{G_{v\varphi}}{1+Z_o/Z_L}}{1+(1+A)L+L_{fb}}\tilde{v}_{\rm ref} - \frac{\frac{Z_o}{1+Z_o/Z_L}}{1+(1+A)L+L_{fb}}\tilde{i}_o \\ &= \frac{G_{vc}F_m\frac{G_{v\varphi}}{1+Z_o/Z_L}}{1+L}\tilde{v}_{\rm ref} - \frac{1}{\frac{1}{Z_\Theta}+\frac{1}{Z_V}}\tilde{i}_o \\ &= G_{vr}\tilde{v}_{\rm ref} - Z'_\Theta\tilde{i}_o \end{aligned} \tag{11}$$

where

$$Z_V = \frac{1}{(1+L)\,H_{fb}F_mF_vn_sG_{i\varphi}}. \tag{12}$$

Thus, compared to the case with PI compensation only, the additional feedback loop further reduces the converter's output impedance by introducing a parallel-connected virtual impedance Z_V. Besides, it can be seen that, with the insertion of the forward-path gain $A = L_{fb}$, the reference-to-output-voltage transfer function G_{vr} of the modified system remains the same as that of the original system shown in Fig. 3. Since the magnitude of Z_V is affected by the converter's loop gain L, which is $\gg 1$ and $\ll 1$ for frequencies below and above the crossover frequency f_{c2}, respectively, the influence of Z_V will also be different in these two frequency regions. In general, it can be assumed in the subsequent discussions that

$$Z_V \approx \begin{cases} \dfrac{1}{LH_{fb}F_mF_vn_sG_{i\varphi}} & f < f_{c2} \\ \dfrac{1}{H_{fb}F_mF_vn_sG_{i\varphi}} & f > f_{c2}. \end{cases} \tag{13}$$

The new equivalent circuit of the DAB dc—dc converter implemented with PI control and virtual-output-impedance shaping is shown in Fig. 7.

1) Proportional Feedback: If the feedback gain H_{fb} is chosen to be a pure number X, the converter's loop gain L can be computed by considering two frequency regions, $f_{c1} < f < f_{c2}$ and $f > f_{c2}$, where L is $\gg 1$ and $\ll 1$, respectively. For $f_{c1} < f < f_{c2}$, we have $G_{vc} \approx K_p$, hence L can be approximated by (14), assuming that $Z_o \ll Z_L$, which is typically true for most converters

$$L = G_{vc}F_mF_vn_s\frac{G_{v\varphi}}{1+Z_o/Z_L} \approx \frac{K_pF_mF_vn_sG_{i\varphi}}{sC_o}. \tag{14}$$

By substituting L from (14) into (13), the virtual impedance introduced by the feedback gain $H_{fb} = X$ can be obtained as given by

$$Z_V \approx \begin{cases} \dfrac{sC_o}{K_pX\left(F_mF_vn_sG_{i\varphi}\right)^2} = sL_{Vp} & f_{c1} < f < f_{c2} \\ \dfrac{1}{XF_mF_vn_sG_{i\varphi}} = R_{Vp} & f > f_{c2}. \end{cases} \tag{15}$$

The result can be viewed as the modification of the converter's original output impedance by the parallel connection of a virtual impedance made up of an inductor L_{Vp} and a resistor R_{Vp}. For $f_{c1} < f < f_{c2}$, the virtual impedance shows an inductive behavior dominated by L_{Vp}. For $f > f_{c2}$, it becomes resistive and is characterized by R_{Vp}. As depicted in Fig. 8, the overall output impedance of the converter can be viewed as the parallel combination of five equivalent circuit elements: R_L, R_Θ, C_Θ, L_{Vp}, R_{Vp}. Their values can be computed from (8) and (15). It should be noted that L_Θ only becomes dominant at low frequencies ($< f_{c1}$) and has been ignored here.

The mathematical expression of the converter's overall output impedance $Z_{\Theta V}$ including the effects of PI compensation and virtual impedance is given by (16). Since the design objective is to reduce the converter's overall output impedance, the virtual impedance should contribute to ensure that the maximum value of the modified converter's output impedance, which occurs when $\mathrm{Im}\left(Z_{\Theta V}^{-1}\right) = 0$, is smaller than its original value $(R_L||R_\Theta)$. From (16), it can be concluded that this requirement is fulfilled for all $X > 0$ since $|Z_{\Theta V}|_{\max} = (R_L||R_\Theta||R_{Vp})$

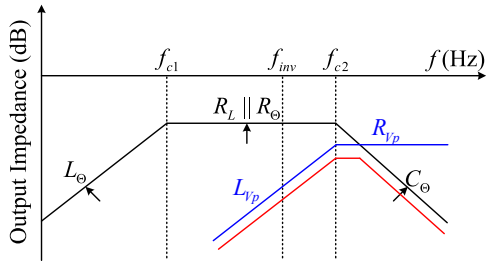

Fig. 9. Closed-loop output impedance of DAB dc–dc converter implemented with PI control and proportional output-voltage feedback.

must be smaller than $(R_L||R_\Theta)$

$$\left|Z_{\Theta V}^{-1}\right| = \left|R_L^{-1} + R_\Theta^{-1} + sC_\Theta + (sL_{Vp})^{-1} + R_{Vp}^{-1}\right| = \left|\left(R_L^{-1} + R_\Theta^{-1} + R_{Vp}^{-1}\right) + j\left(\omega C_\Theta - \frac{1}{\omega L_{Vp}}\right)\right|. \quad (16)$$

However, when the modified converter's output impedance is required to be smaller than its original value at a given frequency f_{inv} below f_{c2} (above f_{c2} the converter's output impedance becomes dominated by C_o and cannot be actively shaped), for example, when it is aimed to minimize the second-harmonic component on the dc bus voltage of an inverter-loaded fuel-cell power conditioning system, the inductive part of the virtual impedance (L_{Vp}) should be selected such that $|sL_{Vp}| \le (R_L||R_\Theta)$. This requires that the proportional feedback gain X fulfills the following criterion:

$$\omega_{\text{inv}} L_{Vp} \le (R_L||R_\Theta) \Rightarrow X \ge \frac{2\pi f_{\text{inv}} C_o}{K_p\,(R_L||R_\Theta)\,(F_m F_v n_s G_{i\varphi})^2}. \quad (17)$$

A typical converter's closed-loop output impedance shaped with X that fulfills this criterion is depicted by the red line plotted in Fig. 9.

2) Derivative Feedback: If the feedback gain H_{fb} is chosen to be a pure derivative term of the form sX, the virtual impedance Z_V can be computed similarly as before by substituting L from (14) and $H_{fb} = sX$ into (13). The result is given by

$$Z_V \approx \begin{cases} \dfrac{C_o}{K_p X\,(F_m F_v n_s G_{i\varphi})^2} = R_{Vd} & f_{c1} < f < f_{c2} \\ \dfrac{1}{sX F_m F_v n_s G_{i\varphi}} = \dfrac{1}{sC_{Vd}} & f > f_{c2}. \end{cases} \quad (18)$$

Hence, the effect of derivative feedback can be viewed as the parallel connection of a virtual impedance made up of a resistor R_{Vd} and a capacitor C_{Vd}. For $f_{c1} < f < f_{c2}$, the virtual impedance shows a resistive behavior dominated by R_{Vd}. For $f > f_{c2}$, it becomes capacitive and is characterized by C_{Vd}. As depicted in Fig. 10, the overall output impedance of the converter can be viewed as the parallel combination of five equivalent circuit elements: R_L, R_Θ, C_Θ, R_{Vd}, C_{Vd}. Their values can be computed from (8) and (18). Again, it should be noted that L_Θ only becomes dominant at low frequencies ($< f_{c1}$) and has been ignored here.

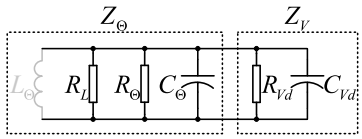

Fig. 10. Equivalent circuit of DAB dc–dc converter implemented with PI control and derivative output-voltage feedback.

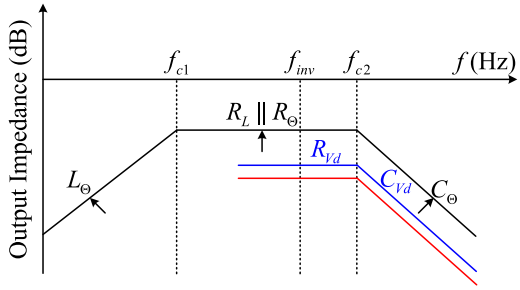

Fig. 11. Closed-loop output impedance of DAB dc–dc converter implemented with PI control and derivative output-voltage feedback.

The mathematical expression of the converter's overall output impedance $Z_{\Theta V}$ including the effects of PI compensation and virtual impedance is given by (19), from which it can be concluded that the maximum value of the modified converter's output impedance is smaller than its original value $(R_L||R_\Theta)$ for all $X > 0$ since $|Z_{\Theta V}|_{\max} = (R_L||R_\Theta||R_{Vd})$ must be smaller than $(R_L||R_\Theta)$

$$\left|Z_{\Theta V}^{-1}\right| = \left|R_L^{-1} + R_\Theta^{-1} + sC_\Theta + R_{Vd}^{-1} + sC_{Vd}\right| = \left|\left(R_L^{-1} + R_\Theta^{-1} + R_{Vd}^{-1}\right) + j\omega\left(C_\Theta + C_{Vd}\right)\right|. \quad (19)$$

However, when the modified converter's output impedance is required to be smaller than its original value at a given frequency f_{inv} below f_{c2}, the resistive part of the virtual impedance (R_{Vd}) should be selected such that $R_{Vd} \le (R_L||R_\Theta)$. This requires that the derivative feedback gain sX fulfills the following criterion:

$$R_{Vd} \le (R_L||R_\Theta) \Rightarrow sX \ge \frac{sC_o}{K_p\,(R_L||R_\Theta)\,(F_m F_v n_s G_{i\varphi})^2}. \quad (20)$$

A typical converter's closed-loop output impedance shaped with X that fulfills this criterion is depicted by the red line plotted in Fig. 11.

3) Integral Feedback: Finally, if the feedback gain H_{fb} is chosen to be a pure integration term of the form X/s, the resulting virtual impedance Z_V takes a more complex form as given by (21). It consists of a parallel connection of a second-order differentiator Z_{Vi} and an inductor L_{Vi}. The overall output impedance of the converter, including the effect of PI compensation, can be viewed as the parallel combination of five equivalent circuit elements: R_L, R_Θ, C_Θ, Z_{Vi}, L_{Vi}, as depicted in Fig. 12. Their values can be computed from (8) and (21). Again, it should be noted that L_Θ only becomes dominant at low frequencies

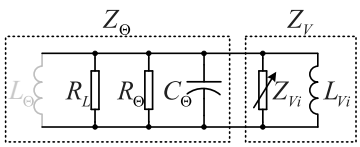

Fig. 12. Equivalent circuit of DAB dc–dc converter implemented with PI control and integral output-voltage feedback.

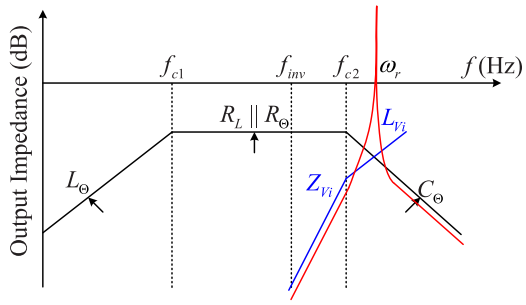

Fig. 13. Closed-loop output impedance of DAB dc–dc converter implemented with PI control and integral output-voltage feedback.

($< f_{c1}$) and has been ignored here

$$Z_V \approx \begin{cases} \dfrac{s^2 C_o}{K_p X \left(F_m F_v n_s G_{i\varphi}\right)^2} = s^2 Z_{Vi} & f_{c1} < f < f_{c2} \\ \dfrac{s}{X F_m F_v n_s G_{i\varphi}} = s L_{Vi} & f > f_{c2}. \end{cases} \tag{21}$$

The mathematical expression of the converter's overall output impedance $Z_{\Theta V}$ including the effects of PI compensation and virtual impedance is given by (22). The maximum value of the modified converter's output impedance occurs when $\mathrm{Im}\left(Z_{\Theta V}^{-1}\right) = 0$, which gives $\omega_r = 1/\sqrt{L_{Vi} C_\Theta}$ and $|Z_{\Theta V}|_{\max} = R_L$. Thus, in contrary to the previous two cases, the maximum value of the modified converter's output impedance is always larger than its original value $(R_L || R_\Theta)$ for all $X > 0$

$$\begin{aligned} \left|Z_{\Theta V}^{-1}\right| &= \left|R_L^{-1} + R_\Theta^{-1} + sC_\Theta + \left(s^2 Z_{Vi}\right)^{-1} + \left(sL_{Vi}\right)^{-1}\right| \\ &= \left|\left(R_L^{-1} + R_\Theta^{-1} - \frac{1}{\omega^2 Z_{Vi}}\right) + j\left(\omega C_\Theta - \frac{1}{\omega L_{Vi}}\right)\right|. \end{aligned} \tag{22}$$

By using a similar approach as the previous two cases, when the modified converter's output impedance is required to be smaller than its original value at a given frequency f_{inv} below f_{c2}, the second-order differentiator $\left(s^2 Z_{Vi}\right)$ should be selected such that $\left|s^2 Z_{Vi}\right| \le (R_L || R_\Theta)$. This requires that the integral feedback gain X/s fulfills the following criterion:

$$\omega_{\mathrm{inv}}^2 Z_{Vi} \le (R_L || R_\Theta) \Rightarrow \frac{X}{s} \ge \frac{4\pi^2 f_{\mathrm{inv}}^2 C_o}{s K_p \left(R_L || R_\Theta\right) \left(F_m F_v n_s G_{i\varphi}\right)^2}. \tag{23}$$

A typical converter's closed-loop output impedance shaped with X that fulfills this criterion is depicted by the red line plotted in Fig. 13.

In summary, all the three basic modes of virtual-output-impedance shaping are capable of reducing the converter's closed-loop output impedance compared to the original value obtained with PI compensation only. Among the three modes, both proportional and derivative feedback result in a smaller overall converter's output impedance over the entire frequency range, since the maximum value of the modified converter's output impedance is constantly smaller than its original value, i.e., $|Z_{\Theta V}|_{\max} < |Z_\Theta|_{\max}$. On the contrary, when integral feedback is employed, it can give rise to a larger output impedance at the frequency ω_r where the output capacitor C_Θ $(= C_o)$ resonates with the virtual inductance L_{Vi}. In particular, it can result in a strong resonant peak under light-load condition when R_L is large, which leads to poor output-voltage regulation. However, since the second-order differentiator Z_{Vi} causes the converter's closed-loop output impedance to fall at –40 dB/dec for $f_{c1} < f < f_{c2}$ and –60 dB/dec for $f < f_{c1}$ with decreasing frequency, it makes integral feedback the most effective mode of virtual-output-impedance shaping to reduce the converter's output impedance and improves its output-voltage regulation over its bandwidth. For applications involving ripple-sensitive renewable energy sources, it also makes the converter effective in absorbing the second-order harmonic component on dc bus voltage. The main problem that remains to be solved in using integral feedback is to minimize the effect of the unwanted resonant peak. This will be discussed next.

4) PI Feedback for Achieving Damped Resonance: The resonant peak produced by pure integral feedback can be compensated by introducing damping into the converter's closed-loop output impedance in the form of virtual resistance. According to Fig. 9, a high-frequency virtual resistance R_{Vp} is introduced when proportional feedback is used. To take advantage of the overall low output impedance offered by integral feedback and the damping function of proportional feedback, a complex feedback gain in the form of $H_{fb} = X/s + Y$ is chosen. Since it has the same transfer function as the PI compensator G_{vc}, there are essentially two PI networks in the converter's feedback loop (G_{vc} and H_{fb}). Hence, for clarity, this feedback configuration is named as the *double-proportional-integral feedback (double-PI)*. By substituting H_{fb} into (13), the overall virtual impedance Z_V can be derived and consists of four elements: Z_{Vi}, L_{Vi}, L_{Vp}, and R_{Vp}

$$Z_V \approx \begin{cases} s^2 Z_{Vi} || sL_{Vp} & f_{c1} < f < f_{c2} \\ sL_{Vi} || R_{Vp} & f > f_{c2} \end{cases} \tag{24}$$

where

$$\begin{aligned} Z_{Vi} &= \frac{C_o}{K_p X \left(F_m F_v n_s G_{i\varphi}\right)^2} \\ L_{Vp} &= \frac{C_o}{K_p Y \left(F_m F_v n_s G_{i\varphi}\right)^2} \\ L_{Vi} &= \frac{1}{X F_m F_v n_s G_{i\varphi}} \\ R_{Vp} &= \frac{1}{Y F_m F_v n_s G_{i\varphi}}. \end{aligned} \tag{25}$$

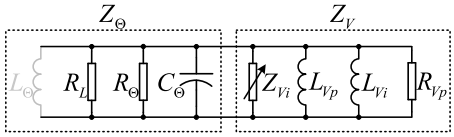

Fig. 14. Closed-loop output impedance of DAB dc–dc converter implemented with double-PI feedback.

With the implementation of double-PI feedback, the converter's overall output impedance $Z_{\Theta V}$ is depicted in Fig. 14 as a parallel combination of seven elements: R_L, R_Θ, C_Θ, Z_{Vi}, L_{Vi}, L_{Vp}, R_{Vp}. The mathematical expression of the overall output impedance of the converter is given by (26) from which two observations can be made

$$\begin{aligned}\left|Z_{\Theta V}^{-1}\right| &= \left|R_L^{-1}+R_\Theta^{-1}+sC_\Theta+\left(s^2Z_{Vi}\right)^{-1}+\left(sL_{Vi}\right)^{-1}\right.\\ &\quad\left.+\ \left(sL_{Vp}\right)+R_{Vp}^{-1}\right|\\ &= \left|\left(R_L^{-1}+R_\Theta^{-1}+R_{Vp}^{-1}-\frac{1}{\omega^2Z_{Vi}}\right)\right.\\ &\quad\left.+\ j\left(\omega C_\Theta-\frac{1}{\omega L_{Vi}}-\frac{1}{\omega L_{Vp}}\right)\right|. \end{aligned}\tag{26}$$

First, the resonant frequency has been shifted to a higher frequency $\omega_{rd}=\sqrt{\left(L_{Vi}+L_{Vp}\right)/\left(C_\Theta L_{Vi}L_{Vp}\right)}$ compared to the undamped resonant frequency ω_r resulting from pure integral feedback only. This has the advantage of shifting the resonant frequency away from the crossover frequency f_{c2} and gives better stability margins. Second, the maximum value of the modified converter's output impedance, which occurs when $\mathrm{Im}\left(Z_{\Theta V}^{-1}\right)=0$, is reduced due to the contribution of R_{Vp}. By imposing the condition $R_{Vp}^{-1}-\left(\omega_{rd}^2Z_{Vi}\right)^{-1}>0$, the damped resonant peak can be suppressed to a value lower than the maximum value of the unmodified converter's output impedance $(R_L||R_\Theta)$. The condition can be met if X and Y fulfill

$$\frac{Y}{X}>\frac{K_pF_mF_vn_sG_{i\varphi}}{\omega_{rd}^2C_o}.\tag{27}$$

With the use of PI feedback, the converter's closed-loop output impedance in the mid-range frequencies $(f_{c1}<f<f_{c2})$ is given by $\left(s^2Z_{Vi}||sL_{Vp}\right)$, which can be written in the more compact form given by

$$s^2Z_{Vi}||sL_{Vp}=\frac{s^2Z_{Vi}}{1+s\left(Y/X\right)}.\tag{28}$$

To design the modified converter's output impedance such that it is smaller than its original value (with PI compensation only) at a given frequency $f_{\mathrm{inv}}\ (=\omega_{\mathrm{inv}}/2\pi)$ below f_{c2}, X and Y should also fulfill the following criterion:

$$\begin{aligned}\frac{\omega_{\mathrm{inv}}^2Z_{Vi}}{\sqrt{1+\omega_{\mathrm{inv}}^2\left(Y/X\right)^2}} &\le \left(R_L||R_\Theta\right)\Rightarrow X^2+\omega_{\mathrm{inv}}^2Y^2\\ &\ge \left[\frac{\omega_{\mathrm{inv}}^2C_o}{K_p\left(R_L||R_\Theta\right)\left(F_mF_vn_sG_{i\varphi}\right)^2}\right]^2.\end{aligned}\tag{29}$$

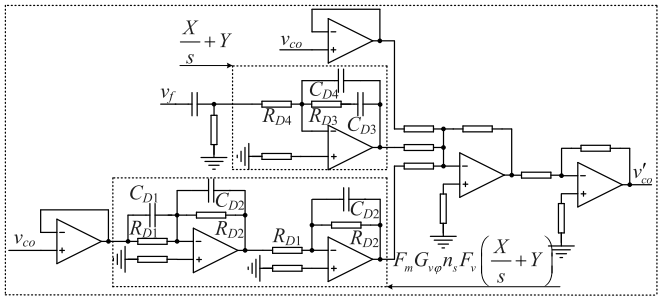

Fig. 15. Practical implementation of double-PI feedback for virtual-output-impedance shaping.

IV. Practical Implementation of Double-PI Feedback

Fig. 15 shows the practical implementation of double-PI feedback for achieving damped resonance in the closed-loop output impedance of DAB dc–dc converter. The feedback gain $H_{fb}=X/s+Y$ is implemented using the inverting amplifier containing R_{D3}, R_{D4}, C_{D3}, and C_{D4}, where $X=1/\left(R_{D4}C_{D3}\right)$ and $Y=R_{D3}/R_{D4}$. The feedback capacitor C_{D4} is added for attenuating high-frequency noise. In order to avoid the saturation of the inverting amplifier's output, the output voltage v_f is sampled using a high-pass filter. The presence of the high-pass filter will not alter the converter's dynamic response and output impedance significantly if its 3-dB frequency is $\ll f_{c1}$. The additional forward-path gain A is implemented using two cascaded integrators containing R_{D1}, R_{D2}, C_{D1}, and C_{D2}. The overall transfer function of the cascaded integrators $H(s)$ is given by

$$H(s)=\frac{1+sR_{D1}C_{D1}}{\left(\frac{R_{D1}}{R_{D2}}\right)^2+s\left(\frac{2R_{D1}^2C_{D2}}{R_{D2}}\right)+s^2\left(R_{D1}C_{D2}\right)^2}.\tag{30}$$

Recall that the additional forward-path gain A should be set to the loop gain of the additional feedback loop L_{fb}. Assuming that $Z_o\ll Z_L$ as usual, A can be approximated by

$$\begin{aligned}A=\ L_{fb} &= F_mF_nn_s\frac{G_{v\varphi}}{1+Z_o/Z_L}\left(\frac{X}{s}+Y\right)\\ &\approx \frac{1+s\left(\frac{Y}{X}\right)}{s^2\left(\frac{C_o}{XF_m\,F_vn_sG_{i\varphi}}\right)}=\frac{1+s\left(\frac{Y}{X}\right)}{s^2L_{Vi}C_o}.\end{aligned}\tag{31}$$

By comparing (30) and (31), the criteria for selecting the values of R_{D1}, C_{D1}, and C_{D2} can be obtained as given by (32). R_{D2} is included to avoid the saturation of the integrators' outputs and should be chosen to be as large as possible ($\gg R_{D1}$) while not saturating the integrators' outputs

$$\begin{aligned}R_{D1}C_{D1} &= \frac{Y}{X}\\ R_{D1}C_{D2} &= \sqrt{L_{Vi}C_o}.\end{aligned}\tag{32}$$

Figs. 16 and 17 compare four cases of the converter's loop gain and closed-loop output impedance with: 1) single-PI (conventional PI); 2) undamped (with $Y=0$) double-PI feedback; 3) damped (with $Y>0$) double-PI feedback; and 4) practical implementation of double-PI feedback. It can be seen that, in the

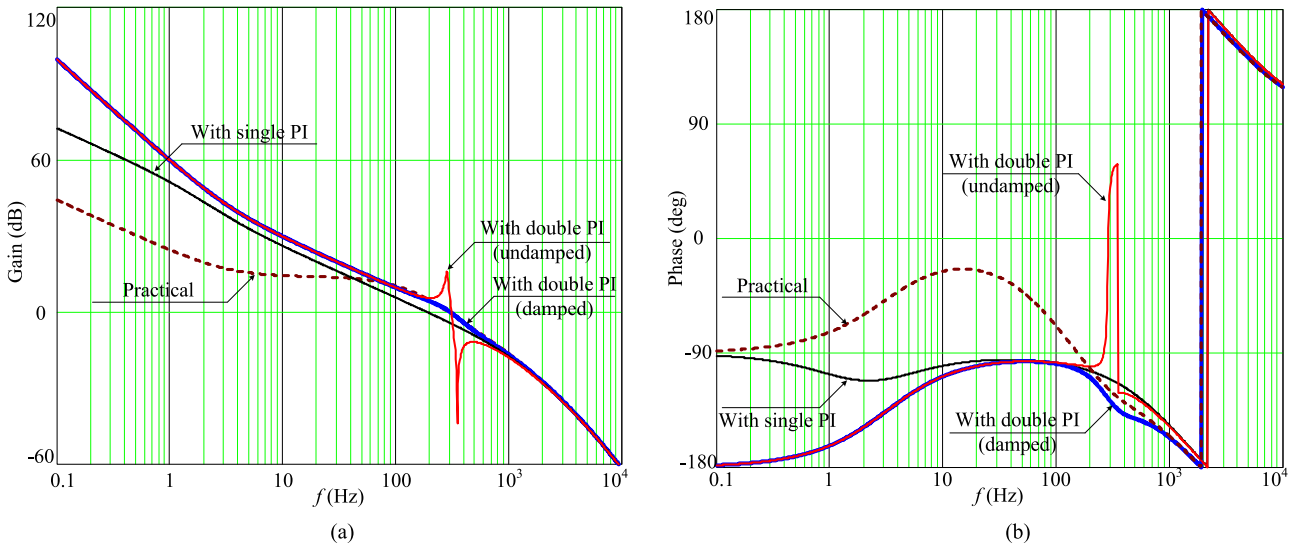

Fig. 16. Bode plots of converter's loop gain with and without virtual-output-impedance shaping.

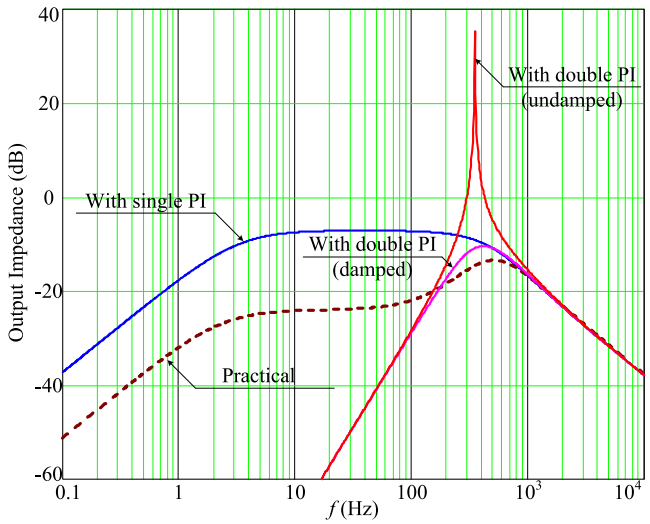

Fig. 17. Plots of converter's closed-loop output impedance with and without virtual-output-impedance shaping.

TABLE I
SPECIFICATIONS OF THE TWO-INPUT BIDIRECTIONAL DAB DC–DC CONVERTER PROTOTYPE

Description	Parameter	Value
Fuel cell's output power	P_{fc}	160 W
Fuel cell's terminal voltage	V_{fc}	20 V
Transformer's leakage inductance (fuel cell branch)	L_{r1}	4.7 μH
Transformer's turn ratio (fuel cell branch)	$N_{p1} : N_{s1}$	1:10
Dc-link capacitor for input half-bridge (fuel cell branch)	C_{p1}	80 μF
Maximum battery power	$P_{\rm bat}$	160 W
Battery's terminal voltage	$V_{\rm bat}$	48 V
Transformer's leakage inductance (battery branch)	L_{r2}	25.5 μH
Transformer's turn ratio (battery branch)	$N_{p2} : N_{s2}$	6:25
Dc-link capacitor for input half-bridge (battery branch)	C_{p2}	5 μF
Dc-link capacitor for secondary half-bridge	C_s	100 μF
Output dc bus voltage	V_o	400 V
Output dc-link capacitor	C_o	20 μF
Switching frequency	f_{sw}	52 kHz

absence of damping, the resonance between the virtual inductor generated by integral feedback L_{Vi} and the output capacitor C_o causes drastic changes in the converter' magnitude and phase responses near the crossover frequency, which potentially leads to instability or difficulty in compensator design. It also introduces a strong peak in the converter's output impedance, which leads to poor output-voltage regulation as discussed. With the assistance of damping provided by proportional feedback, the resonance peak is strongly attenuated and both magnitude and phase responses of the converter change gradually over a wider frequency range. An additional benefit derived from this is that the requirement for small virtual inductor in order to shift the resonance peak to high frequencies (considerably higher than the crossover frequency), which requires a large X, becomes less stringent and its value can be selected for achieving a specific output impedance $s^2 L_{Vi}$, which also depends on X, at a given frequency $f_{\rm inv}$, such as the second-harmonic frequency generated by inverter load.

V. EXPERIMENTAL VERIFICATION

In this section, the performance of the proposed double-PI feedback for suppression of second-harmonic component on dc bus voltage is evaluated. For this purpose, a prototype of two-input (fuel cell and energy storage) bidirectional DAB dc–dc converter driving an inverter load is constructed with the specifications listed in Table I. In the experimental system, the fuel cell unit is emulated using a dc power supply that delivers constant power to the system. To avoid the supply of second-harmonic current from the fuel cell branch, its closed-loop bandwidth is designed to be 7 Hz, i.e., $<$ 1/10 of the second-harmonic frequency at 100 Hz. For the energy storage branch, a battery bank made of four 12-V, 18-Ah series-connected lead-acid batteries is used. The closed-loop bandwidth of the battery branch is designed to be approximately 190 Hz. The inverter is a

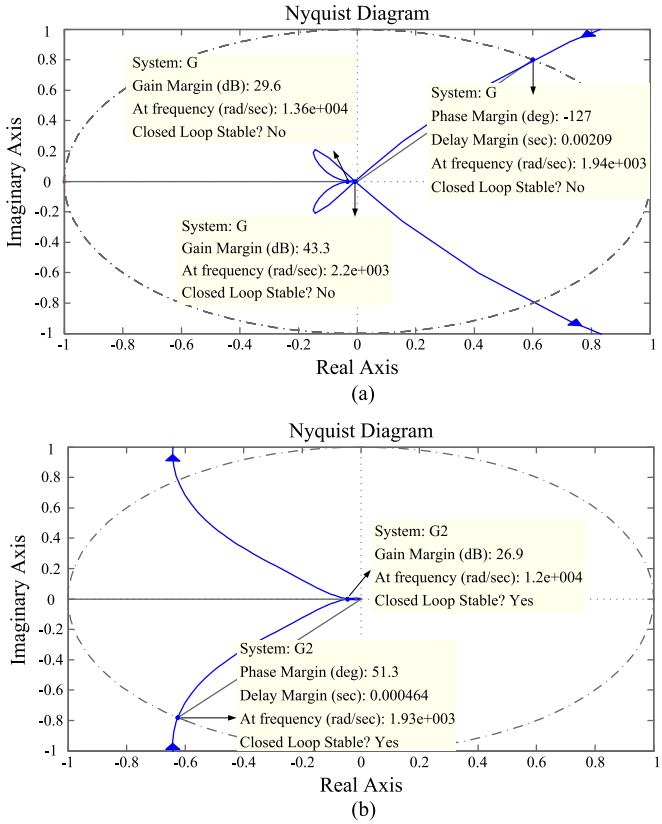

Fig. 18. Nyquist plots of converter with (a) undamped ($Y = 0$); and (b) damped ($Y > 0$) double-PI feedback.

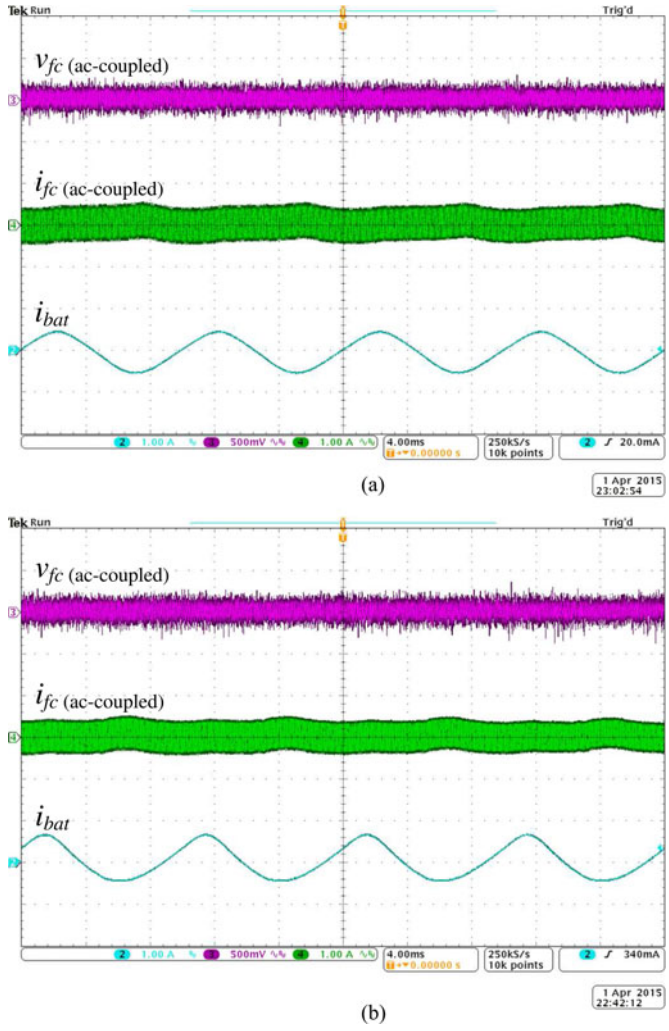

Fig. 19. Static converter waveforms with (a) single-PI (conventional PI); and (b) double-PI feedback. ($v_{\rm fc}$: fuel cell's output voltage; $i_{\rm fc}$: fuel cell's output current; $i_{\rm bat}$: battery's output current).

conventional one based on full-bridge topology driven by sinusoidal pulse width modulation. Note that a small output dc-link capacitor (20 μF) is intentionally selected to generate a significant amount of second-harmonic component on the dc bus voltage so that its suppression by virtual-output-impedance shaping can be more clearly visualized during experimental measurements.

To evaluate the effectiveness of the damping function of proportional feedback, the virtual inductor L_{Vi} generated by integral feedback is intentionally selected to be 165 μH, so that a strong resonance peak is generated at around 350 Hz in the absence of damping, as shown in Fig. 16. Due to its proximity to the crossover frequency (190 Hz), the unsuppressed resonance peak is expected to have negative impact on the converter's closed-loop stability and complicate the compensator design. This is verified by applying Nyquist stability criterion on an undamped system using integral feedback only for output-impedance shaping, where the system is found to be unstable [see Fig. 18(a)]. On the other hand, stability is regained when the system is damped by using PI feedback [see Fig. 18(b)].

The steady-state waveforms of the DAB converter implemented with single-PI (conventional PI) and double-PI feedback are shown in Figs. 19 and 20. In Fig. 19, $v_{\rm fc}$ and $i_{\rm fc}$ is the fuel cell's output voltage and output current, respectively, and $i_{\rm bat}$ is the battery's output current. It should be apparent that in all cases no ac current at the second-harmonic frequency is drawn from the fuel cell branch due to its very small closed-loop bandwidth; hence, second-harmonic current is mainly delivered by the dc-link capacitor and the battery branch. In Fig. 20, $v_{o(\rm dc)}$ is the dc bus voltage and i_b' is the DAB dc–dc converter's output current. For the dc bus voltage, only the ac-coupled waveform is shown in order to give a magnified and clear view of the second-harmonic (100-Hz) component.

In comparison to the converter using single-PI feedback only, the implementation of virtual-output-impedance shaping in the form of PI feedback has clearly reduced the converter's closed-loop output impedance, as shown by the strongly suppressed second-harmonic component on the dc bus voltage. The quantitative changes in the size of the second-harmonic component can be more directly visualized from the FFT spectra of the dc bus voltage waveforms shown in Fig. 21(a) and (b). In comparison to the case with single-PI feedback, the amplitude of the second-harmonic component has been reduced by 85.5%. The measured trend is in very close agreement with the percentage reduction in the converter's closed-loop output impedance predicted

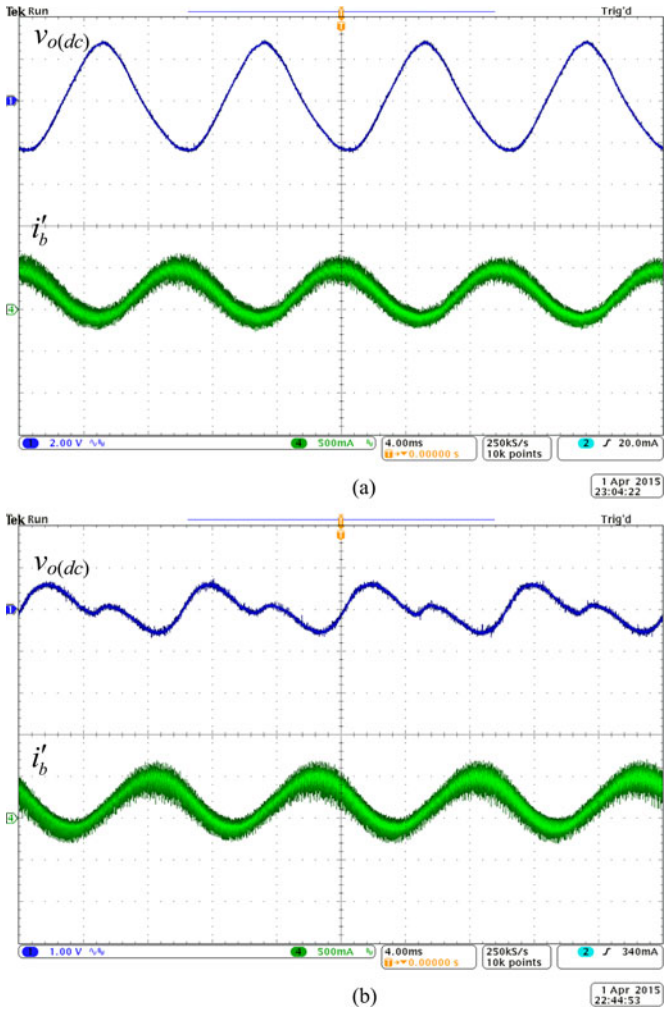

Fig. 20. Static converter waveforms with (a) single-PI (conventional PI); and (b) double-PI feedback. ($v_{o(dc)}$: dc bus voltage; i'_b: DAB converter's output current).

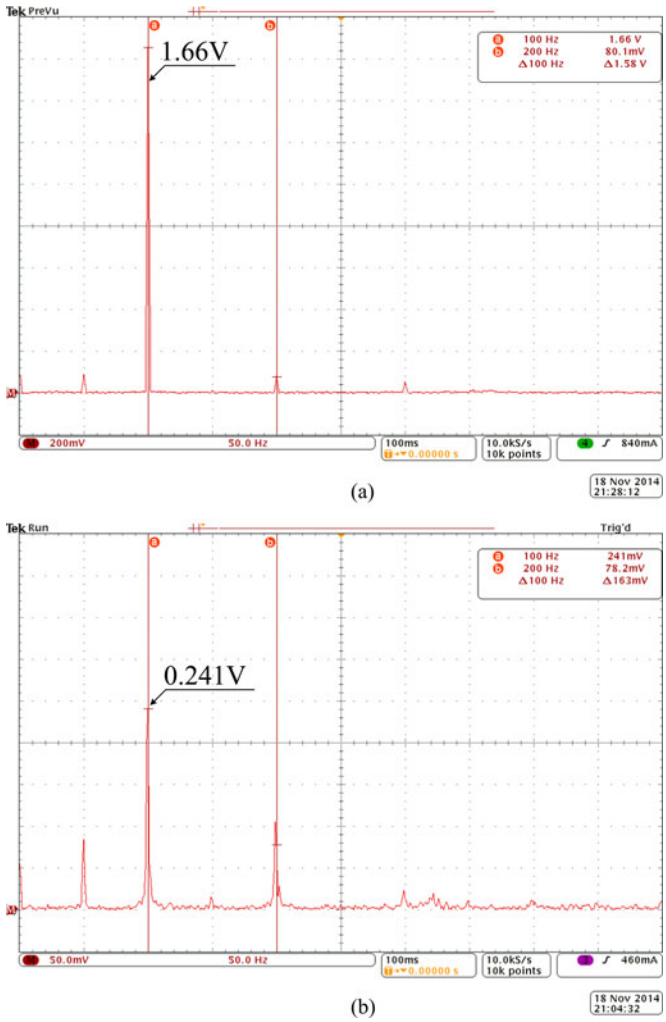

Fig. 21. FFT analysis of the dc bus voltage with (a) single-PI (conventional PI); and (b) double-PI feedback.

by theoretical analysis, which gives 85.3% (computed from the difference between $-7.45\,\mathrm{dB}\cdot\Omega$ for single-PI feedback and $-24.08\,\mathrm{dB}\cdot\Omega$ for double-PI feedback) according to Fig. 17.

Finally, the dynamic response of the converter implemented with single-PI feedback and double-PI feedback were tested and the results are shown in Fig. 22(a) and (b). In both cases, the inverter's load was stepped from half-load to full-load. It can be seen that before the step-load occurred, the average battery's current was negative, indicating that the battery bank was charged by the fuel cell branch. After the step-load occurred, the average battery's current became approximately zero as the fuel cell branch's output power was balanced by the inverter's load power. In comparison to the converter using single-PI feedback only, the employment of virtual-output-impedance shaping compensated with additional forward-path gain (A) ensures that the system is stable and its dynamic response remains unchanged, that is, it is affected only by the compensator design (G_{vc}) of the original system.

VI. Conclusion

In conclusion, a two-input (fuel cell and battery) bidirectional DAB dc–dc converter system employing virtual-output-impedance shaping for minimizing second-harmonic distortion on dc bus voltage is presented. Focusing on the energy storage branch which is responsible for dc bus voltage regulation, the closed-loop output impedance of the converter-interfaced energy storage is carefully analyzed, both in the absence of and with the inclusion of virtual-output-impedance shaping. The three basic modes of output-voltage feedback, i.e., proportional, derivative, integral, are shown to interact differently with the existing output-voltage feedback loop and give rise to various output-impedance characteristics. Among them, integral feedback is shown to be advantageous in minimizing the energy storage branch's output impedance for second-harmonic power absorption due to its−40– −60 dB/dec roll-off within the converter's bandwidth. It is also shown that the resonant peak that it generates upon resonance with the converter's output capacitor has the potential of destabilizing the system and complicating compensator design. The damping of the resonant peak by the

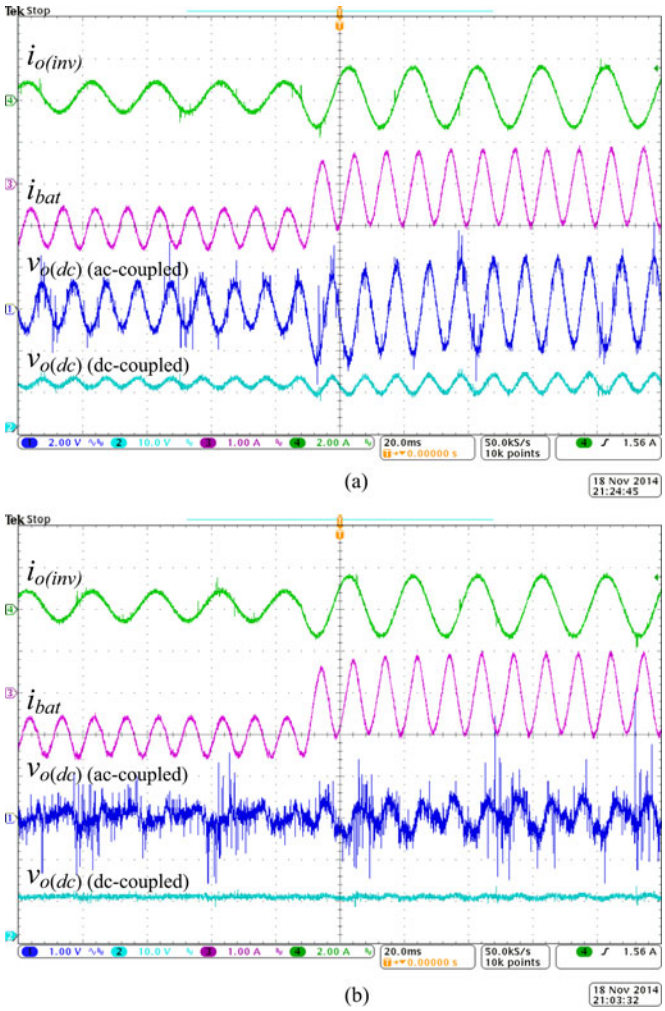

Fig. 22. Dynamic converter waveforms with (a) single-PI (conventional PI); and (b) double-PI feedback.

inclusion of proportional feedback provides an effective solution to mitigating the problem. Thus, in addition to the existing PI compensator, two PI networks are used for achieving extremely small closed-loop output impedance of the energy storage. Experimental results show that the second-harmonic ripple size has decreased by 85.5% upon the implementation of the proposed double-PI feedback method.

REFERENCES

[1] R. W. A. A. De Doncker, D. M.Divan, and M. H. Kheraluwala, "A three-phase soft-switched high-power-density dc/dc converter for high-power applications," *IEEE Trans. Ind. Appl.*, vol. 27, no. 1, pp. 63–73, Jan. 1991.

[2] M. H. Kheraluwala, R. W. Gascoigne, D. M. Divan, and E. D. Baumann, "Performance characterization of a high-power dual active bridge DC-to-DC converter," *IEEE Trans. Ind. Appl.*, vol. 28, no. 6, pp. 1294–1301, Nov. 1992.

[3] G. G. Oggier, G. O. Garcia, and A. R. Oliva, "Switching control strategy to minimize dual active bridge converter losses," *IEEE Trans. Power Electron.*, vol. 24, no. 7, pp. 1826–1838, Jul. 2009.

[4] G. G. Oggier, G. O. Garcia, and A. R. Oliva, "Modulation strategy to operate the dual active bridge DC–DC converter under soft switching in the whole operating range," *IEEE Trans. Power Electron.*, vol. 26, no. 4, pp. 1228–1236, Apr. 2011.

[5] B. Zhao, Q. Yu, and W. Sun, "Extended-phase-shift control of isolated bidirectional DC–DC converter for power distribution in microgrid," *IEEE Trans. Power Electron.*, vol. 27, no. 11, pp. 4667–4680, Nov. 2012.

[6] H. Bai and C. Mi, "Eliminate reactive power and increase system efficiency of isolated bidirectional dual-active-bridge DC–DC converters using novel dual-phase-shift control," *IEEE Trans. Power Electron.*, vol. 23, no. 6, pp. 2905–2914, Nov. 2008.

[7] F. Krismer and J. W. Kolar, "Accurate small-signal model for the digital control of an automotive bidirectional dual active bridge," *IEEE Trans. Power Electron.*, vol. 24, no. 12, pp. 2756–2768, Dec. 2009.

[8] F. Krismer and J. W. Kolar, "Efficiency-optimized high-current dual active bridge converter for automotive applications," *IEEE Trans. Power Electron.*, vol. 59, no. 7, pp. 2745–2760, Jul. 2012.

[9] H. Zhou and A. M. Khambadkone, "Hybrid modulation for dual-active-bridge bidirectional converter with extended power range for ultracapacitor application," *IEEE Trans. Ind. Appl.*, vol. 45, no. 4, pp. 1434–1442, Jul. 2009.

[10] Y. Du, S. M. Lukic, B. S. Jacobson, and A. Q. Huang, "Modulation technique to reverse power flow for the isolated series resonant DC–DC converter with clamped capacitor voltage," *IEEE Trans. Ind. Electron.*, vol. 59, no. 12, pp. 4617–4628, Dec. 2012.

[11] K. Wu, C. W. de Silva, and W. G. Dunford, "Stability analysis of isolated bidirectional dual active full-bridge DC–DC converter with triple phase-shift control," *IEEE Trans. Power Electron.*, vol. 27, no. 4, pp. 2007–2017, Apr. 2012.

[12] A. K. Jain and R. Ayyanar, "PWM control of dual active bridge: Comprehensive analysis and experimental verification," *IEEE Trans. Power Electron.*, vol. 26, no. 4, pp. 1215–1227, Apr. 2011.

[13] H. Tao, J. L. Duarte, and M. A. M. Hendrix, "Three-Port triple-half-bridge bidirectional converter with zero-voltage switching," *IEEE Trans. Power Electron.*, vol. 23, no. 2, pp. 782–792, Mar. 2008.

[14] G. D. Demetriades and H. P. Nee, "Dynamic modeling of the dual-active bridge topology for high-power applications," in *Power Electron. Spec. Conf.*, Jun. 15–19, 2008, pp. 457–464.

[15] C. Zhao, S. D. Round, and J. W. Kolar, "Full-Order averaging modelling of zero-voltage-switching phase-shift bidirectional DC–DC converters," *IET Power Electron.*, vol. 3, no. 3, pp. 400–410, May 2010.

[16] H. Qin and J. W. Kimball, "Generalized average modeling of dual active bridge DC–DC converter," *IEEE Trans. Power Electron.*, vol. 27, no. 4, pp. 2078–2084, Apr. 2012.

[17] G. Guidi, M. Pavlovsky, A. Kawamura, T. Imakubo, and Y. Sasaki, "Improvement of light load efficiency of dual active bridge DC–DC converter by using dual leakage transformer and variable frequency," in *Proc. Energy Convers. Congr. Expo.*, Sep. 12–16, 2010, pp. 830–837.

[18] Y. Du, S. Baek, B. Bhattacharya, and A. Q. Huang, "High-Voltage high-frequency transformer design for a 7.2 kV to 120 V/240 V 20 kVA solid state transformer," in *Proc. 36th Annu. Conf. IEEE Ind. Electron. Soc.*, Nove. 7–10, 2010, pp. 493–498.

[19] B. Zhao, Q. Song, W. Liu, and Y. Sun, "A synthetic discrete design methodology of high-frequency isolated bidirectional DC/DC converter for grid-connected battery energy storage system using advanced components," *IEEE Trans. Ind. Electron.*, vol. 61, no. 10, pp. 5402–5410, Oct. 2014.

[20] A. Payman, S. Pierfederici, and F. Meibody-Tabar, "Energy management in a fuel cell/supercapacitor multisource/multiload electrical hybrid system," *IEEE Trans. Power Electron.*, vol. 24, no. 12, pp. 2681–2691, Dec. 2009.

[21] H. Zhou, T. Bhattacharya, D. Tran, T. Siew, and A. Khambadkone, "Composite energy storage system involving battery and ultracapacitor with dynamic energy management in microgrid applications," *IEEE Trans. Power Electron.*, vol. 26, no. 3, pp. 923–930, Mar. 2011.

[22] G. Su and F. Peng, "A reduced-part, triple-voltage DC–DC converter for EV/HEV power management," *IEEE Trans. Power Electron.*, vol. 24, no. 10, pp. 2406–2410, Oct. 2009.

[23] H. Tao, A. Kotsopoulos, J. Duarte, and M. Hendrix, "Family of multiport bidirectional DC–DC converters," *IEEE Proc. Electric Power Appl.*, vol. 153, no. 3, pp. 451–458, May 2006.

[24] H. Al-Atrash, F. Tian, and I. Batarseh, "Tri-Modal half-bridge converter topology for three-port interface," *IEEE Trans. Power Electron.*, vol. 22, no. 1, pp. 341–345, Jan. 2007.

[25] H. Al-Atrash and I. Batarseh, "Boost-Integrated phase-shift full-bridge converter for three-port interface," in *Proc. IEEE Power Electron. Spec. Conf.*, 17–21 Jun 2007, pp. 2313–2321.

[26] Z. Ding, C. Yang, Z. Zhang, C. Wang, and S. Xie, "A novel soft-switching multiport bidirectional DC–DC converter for hybrid energy storage

system," *IEEE Trans. Power Electron.*, vol. 29, no. 4, pp. 1595–1609, Apr. 2014.
[27] W. Li, J. Xiao, Y. Zhao, and X. He, "PWM plus phase angle shift (PPAS) control scheme for combined multiport DC/DC converters," *IEEE Trans. Power Electron.*, vol. 27, no. 3, pp. 1479–1489, Mar. 2012.
[28] Z. Zhang, Z. Ouyang, O. Thomsen, and M. Andersen, "Analysis and design of a bidirectional isolated DC–DC converter for fuel cells and supercapacitors hybrid system," *IEEE Trans. Power Electron.*, vol. 27, no. 2, pp. 848–859, Feb. 2012.
[29] H. Wu, R. Chen, J. Zhang, Y. Xing, and H. Hu, "A family of three-port half-bridge converters for a stand-alone renewable power system," *IEEE Trans. Power Electron.*, vol. 26, no. 9, pp. 2697–2706, Sep. 2011.
[30] H. Wu, K. Sun, R. Chen, H. Hu, and Y. Xing, "Full-bridge three-port converters with wide input voltage range for renewable power systems," *IEEE Trans. Power Electron.*, vol. 27, no. 9, pp. 3965–3974, Sep. 2012.
[31] Z. Qian, O. Abdel-Rahman, H. Al-Atrash, and I. Batarseh, "Modeling and control of three-port DC/DC converter interface for satellite applications," *IEEE Trans. Power Electron.*, vol. 25, no. 3, pp. 637–649, Mar. 2010.
[32] J. Duarte, M. Hendrix, and M. Simoes, "Three-Port bidirectional converter for hybrid fuel cell systems," *IEEE Trans. Power Electron.*, vol. 22, no. 2, pp. 480–487, Mar. 2007.
[33] H. Tao, A. Kotsopoulos, J. Duarte, and M. Hendrix, "Transformer-coupled multiport ZVS bidirectional DC–DC converter with wide input range," *IEEE Trans. Power Electron.*, vol. 23, no. 2, pp. 771–781, Mar. 2008.
[34] C. Zhao, S. D. Round, and J. W. Kolar, "An isolated three-port bidirectional DC–DC converter with decoupled power flow management," *IEEE Trans. Power Electron.*, vol. 23, no. 5, pp. 2443–2453, Sep. 2008.
[35] D. Liu and H. Li, "A ZVS Bi-Directional DC–DC converter for multiple energy storage elements," *IEEE Trans. Power Electron.*, vol. 21, no. 5, pp. 1513–1517, Sep. 2006.
[36] H. Krishnaswami and N. Mohan, "Three-port series-resonant DC–DC converter to interface renewable energy sources with bidirectional load and energy storage ports," *IEEE Trans. Power Electron.*, vol. 24, no. 10, pp. 2289–2297, Oct. 2009.
[37] L. Cao, K. H. Loo, and Y. M. Lai, "Frequency-Adaptive filtering of low-frequency harmonic current in fuel cell power conditioning systems," *IEEE Trans. Power Electron.*, vol. 30, no. 4, pp. 1966–1978, Apr. 2015.
[38] L. Cao, K. H. Loo, and Y. M. Lai, "Systematic derivation of a family of output impedance shaping methods for power converters–a case study using fuel-cell-battery-powered single-phase inverter system," *IEEE Trans. Power Electron.* (early access).

Lingling Cao (S'13) received the B.S. and M.S. degrees in electrical engineering from the Nanjing University of Aeronautics and Astronautics, Nanjing, China, in 2008 and 2011, respectively. She is currently working toward the Ph.D. degree in the Hong Kong Polytechnic University, Hong Kong.

Her research interests include design and control of power electronic converters for fuel cell power conditioning systems.

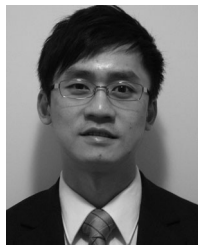

K. H. Loo (S'97–M'99) received the B.Eng. (with Hons.) in electronic engineering and the Ph.D. degree from the University of Sheffield, Sheffield, U.K., in 1999 and 2002, respectively.

From 2002 to 2004, he was the Japan Society for the Promotion of Science Postdoctoral Fellow at the Ehime University, Japan. In 2006, he joined the Hong Kong Polytechnic University as an Instructor in the Faculty of Engineering. He is currently an Assistant Professor in the Department of Electronic and Information Engineering, Hong Kong Polytechnic University. He has been an Associate Editor in the IEEE TRANSACTIONS ON ENERGY CONVERSION since 2013. His research interests include power electronics for LED lighting and renewable energy systems.

Y. M. Lai (M'92) received the B.Eng. degree in electrical engineering from the University of Western Australia, Perth, W.A., Australia, in 1983, the M.Eng.Sc. degree in electrical engineering from the University of Sydney, Sydney, N.S.W., Australia, in 1986, and the Ph.D. degree from Brunel University, London, U.K., in 1997.

He is currently an Associate Professor with the Hong Kong Polytechnic University, Hong Kong. His research interests include computer-aided design of power electronics and nonlinear dynamics.